



# Variability of the Great Disk Shadow in Serpens

Klaus M. Pontoppidan<sup>1</sup> , Joel D. Green<sup>1</sup> , Tyler A. Pauly<sup>1</sup> , Colette Salyk<sup>2</sup> , and Joseph DePasquale<sup>1</sup>

<sup>1</sup>Space Telescope Science Institute, 3700 San Martin Drive, Baltimore, MD 21218, USA; [pontoppi@stsci.edu](mailto:pontoppi@stsci.edu)

<sup>2</sup>Vassar College, 124 Raymond Avenue, Poughkeepsie, NY 12604, USA

Received 2020 February 26; revised 2020 May 6; accepted 2020 May 8; published 2020 June 25

## Abstract

We present dual-epoch Hubble Space Telescope imaging of the great disk shadow in the Serpens star-forming region. The near-infrared images show strong variability of the disk shadow, revealing dynamics of the inner disk on timescales of months. The Great Shadow is projected onto the Serpens reflection nebula by an unresolved protoplanetary disk surrounding the young intermediate-mass star SVS2/CK3/EC82. Since the shadow extends out to a distance of at least 17,000 au, corresponding to a light-travel time of 0.24 yr, the images may reveal detailed changes in the disk scale height and position angle on timescales as short as a day, corresponding to the angular resolution of the images, and up to the 1.11 yr span between two observing epochs. We present a basic retrieval of temporal changes in the disk density structure, based on the images. We find that the inner disk changes position angle on timescales of months, and that the change is not axisymmetric, suggesting the presence of a non-axisymmetric dynamical forcing on  $\sim 1$  au size scales. We consider two different scenarios, one in which a quadrupolar disk warp orbits the central star, and one in which an unequal-mass binary orbiting out of the disk plane displaces the photocenter relative to the shadowing disk. Continued space-based monitoring of the great disk shadow is required to distinguish between these scenarios, and could provide unique and detailed insight into the dynamics of inner protoplanetary disks not available through other means.

*Unified Astronomy Thesaurus concepts:* [Protoplanetary disks \(1300\)](#); [Reverberation mapping \(2019\)](#); [Exoplanet formation \(492\)](#)

*Supporting material:* animation

## 1. Introduction

Pre-main-sequence stars younger than 1–2 Myr often illuminate nearby dust from their natal molecular cloud (Kenyon & Hartmann 1995). This material could originate from a remnant envelope of the young star itself, or could be a quiescent part of the molecular cloud encountered by the young star after traveling a significant distance from its birthplace (e.g., Britt et al. 2016). Indeed, a young star may cross its parent cluster within  $\sim 1$  Myr (Kraus & Hillenbrand 2008; Zari et al. 2019), which is significantly less than the lifetime of the parent molecular cloud. It is plausible that many young stars will illuminate quiescent parts of a cloud at some point in their lifetime.

### 1.1. Disk Shadows

Pre-main-sequence stars are typically surrounded by protoplanetary disks, and since such disks are generally highly optically thick at optical/near-infrared (NIR) wavelengths, they may cast shadows on their surroundings. Such disk shadows have been observed on a wide range of angular scales; recently, high-contrast imaging has revealed shadows cast on outer disks by misaligned inner disks on subarcsecond scales (e.g., Marino et al. 2015; Benisty et al. 2018; Casassus et al. 2018). Such shadows reveal that angular distortions are common in inner disks. This is consistent with the existence of a class of self-shadowed disks in which the inner disk scale height is higher than that of the outer disk, leading to a general shadowing and related cooling of the outer disk (Dullemond & Dominik 2004; Dong 2015). A related type of disk shadow, but on a vastly larger angular scale of arcminutes, are shadows cast on large-scale reflection nebulae. These great disk shadows can occur if a young, usually spatially unresolved, star-disk system is

illuminating a reflection nebula, and are especially apparent for systems viewed close to edge-on (Hodapp et al. 2004; Pontoppidan & Dullemond 2005). Neither of these two types of disk shadow should be confused with silhouette disks that obscure background nebulosity, such as the Orion proplyds (O’dell 1998), or dark dust lanes in isolated edge-on disks (Burrows et al. 1996; Stapelfeldt et al. 1998; Duchêne et al. 2010). The projection of the disk onto a large reflection nebula can greatly magnify a small structure in the obscuring disk. Indeed, the apparent angular size of great disk shadows is only limited by the size of the reflection nebula illuminated by the central star, and may be orders of magnitude larger than the protoplanetary disk itself. Great disk shadows therefore present a unique opportunity to explore the geometry of disks on scales otherwise not resolved by direct imaging, primarily the disk scale height, inclination, and position angle.

### 1.2. The Great Disk Shadow in Serpens

One of the most iconic disk shadows is the great shadow in the main core of the Serpens star-forming region (Figure 1), illuminated by the young intermediate-mass star EC 82 (HBC 672/CK 3/SVS 2; Pontoppidan & Dullemond 2005). Indeed, EC 82 is the dominant illuminating source in the Serpens main core reflection nebula (Sugitani et al. 2010). Because the NIR spectrum of EC 82 is strongly veiled, its effective temperature is uncertain (see discussion in Gorlova et al. 2010). Winston et al. (2009) report an effective temperature of 3900 K (K8) with *H*- and *K*-band spectra, but both Doppmann et al. (2005) and Gorlova et al. (2010) find that the NIR spectrum of EC 82 is too veiled to yield a reliable effective temperature, and the featureless spectrum of EC 82 is therefore also consistent with an early-type photosphere. Pontoppidan & Dullemond (2005) used a detailed

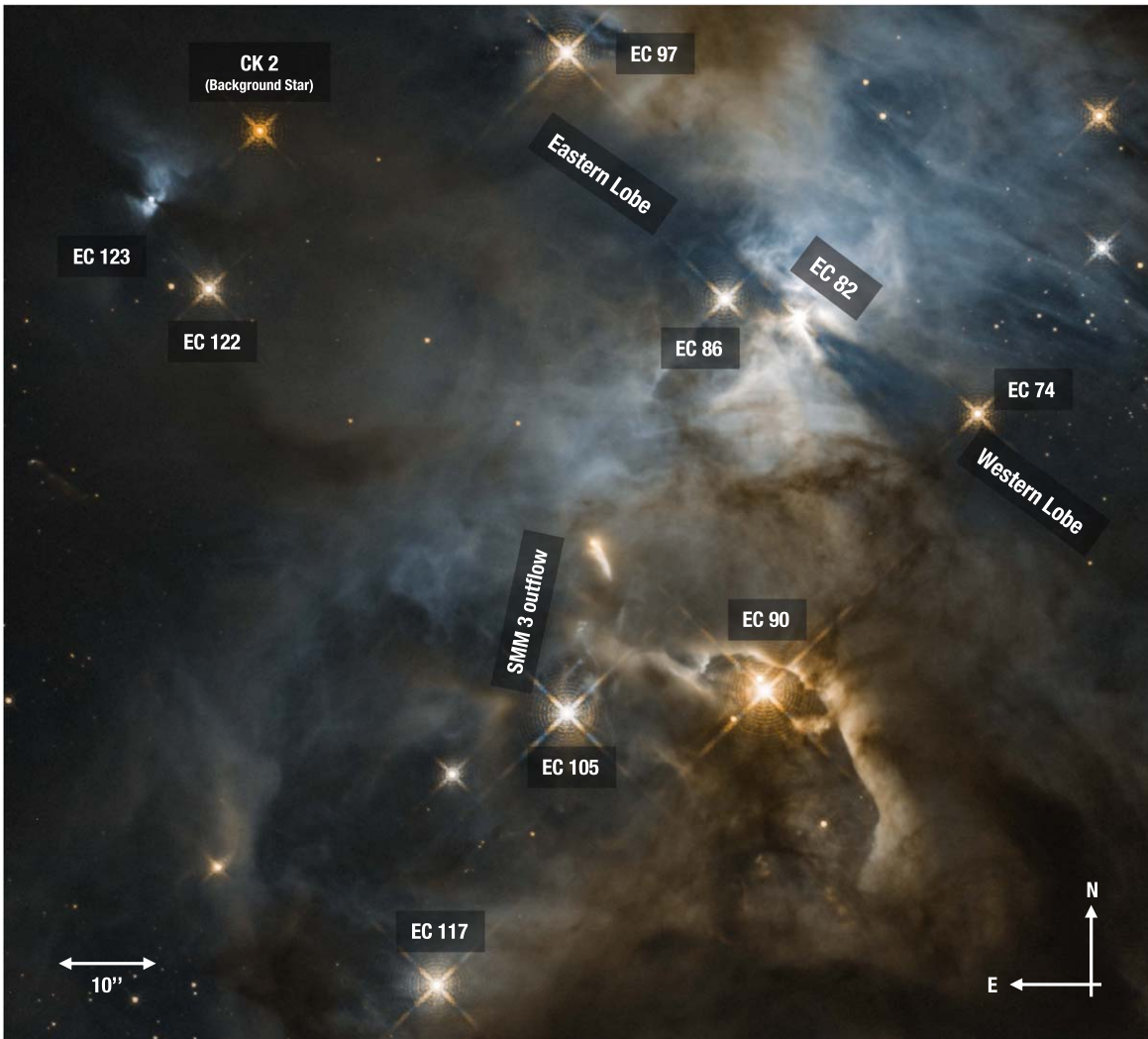


**Figure 1.** Annotated two-color WFC3 image of the Serpens core in the vicinity of EC 82, in F125W (blue) and F164N (red).

radiative transfer model of the shadow, spectral energy distribution (SED), and reflection nebula to estimate a luminosity of  $30 L_{\odot}$  (scaled to the VLBI distance of  $436 \pm 9$  pc (Ortiz-León et al. 2017) from their assumed distance of 250 pc). Dunham et al. (2015) reported a somewhat lower luminosity of  $16 L_{\odot}$  based on the SED. This difference may be due to the two-dimensional model in Pontoppidan & Dullemond (2005) taking into account the edge-on geometry of the disk, which leads to a significant suppression of the optical to mid-infrared parts of the SED. Using the pre-main-sequence evolutionary track of Siess et al. (2000) and assuming an age of 1–2 Myr predicts effective temperatures of 5400–6100 K, and stellar masses of  $2.5\text{--}3.0 M_{\odot}$ . That is, based in the accurate VLBI distance, EC 82 is likely a young intermediate-mass star, and either an actual, or a precursor to, a Herbig Ae star.

In this paper we present NIR Hubble Space Telescope/Wide-Field Camera 3 (HST-WFC3) imaging of the Serpens disk shadow from EC 82 over two epochs separated by 404 days, and demonstrate that the shadow varies significantly over this timescale. We find that the angle of the shadow changed by several degrees, providing a unique probe of the dynamics of the inner disk of this system. We also find evidence for significant variability within at least one of the two epochs on timescales of  $\sim 1$  month.

### 1.3. Time-variable Shadows

Time-variable self-shadowing of outer protoplanetary disks has been observed by direct imaging in a variety of systems. Such phenomena may be related to that described here, but the order-of-magnitude magnification provided by the Serpens reflection nebula allows investigation of phenomena on spatial scales not possible in directly observed disks. For instance, the HH30 edge-on disk exhibited asymmetry and variability when observed by HST between 1994 and 2005 (Watson & Stapelfeldt 2007), with possible (but poorly constrained) periodicity on timescales less than 1 yr. Using HST/Space Telescope Imaging Spectrograph and Near Infrared Camera and Multi-Object Spectrometer (NICMOS) imaging, Debes et al. (2017) found azimuthal asymmetry associated with  $\sim 15.9$  yr periodic variability in the more evolved TW Hya system between 1998 and 2005. In that case, they hypothesized that the disk interior to 1 au was inclined and precessing relative to the outer disk, causing a shadow on the outer disk. They invoke an external perturber as the cause of the disk warp or misalignment. Using Very Large Telescope (VLT)/Spectro-Polarimetric High-contrast Exoplanet REsearch (SPHERE), Pinilla et al. (2018) found a periodic outer disk shadowing around the Dipper Star RXJ1604.3-2130, consistent with

**Table 1**  
Observing Log

| Date        | Instrument | Filter | Exposure time<br>(s) |
|-------------|------------|--------|----------------------|
| 2017 Jul 22 | WFC3       | F160W  | 1597                 |
| 2018 Aug 30 | WFC3       | F164N  | 5998                 |
| 2018 Aug 30 | WFC3       | F125W  | 1798                 |

observed dimming events. In this case, either a planetary-mass companion or magnetic field alignment effects could be invoked. In each case, the variability of the shadow over a large spatial scale (tens of astronomical units) represented a much smaller scale ( $\sim 1$  au) perturbation in the disk.

In Section 2, we describe the two epochs of observations. In Section 3, we quantify the shadow morphology and its variability using the high resolution and reproducibility of the HST data. Finally, in Section 4, we discuss the implications for the EC 82 protoplanetary disk.

## 2. Observations

EC 82 was first observed by WFC3 on 2017 July 22 as part of HST program 14181 using the F160W filter. The region was subsequently observed in the F125W and F164N filters on 2018 August 30 as part of program 15597. These observations covered a  $123'' \times 136''$  field of view, at a resolution of  $0''.13$  per pixel. For the F160W observation, the STEP50 sample sequence with 14 non-destructive detector reads was used, while the STEP400 sequence with 14 reads was used for the F164N narrow-band image. Table 1 summarizes the observations.

Both data sets were downloaded from the Mikulski Archive for Space Telescopes in FLT format, as output from the `calwf3` data reduction pipeline, which includes basic calibration of the raw data, including bias and dark current subtraction, linearity correction, flat-fielding, bad pixel masking, and cosmic-ray removal. Each image was processed through the `Drizzlepac` package, using `Tweakreg` for individual dithered exposure alignment, and `Astrodrizzle` to combine the individual exposures. The `Astrodrizzle` processing included sky subtraction using a median statistic, along with further cosmic-ray reduction using `driz_cr`, finally creating a drizzled, combined image with an output pixel size of  $0''.08$ .

Figure 1 shows the two-color composite of the Serpens core (F125W, blue and F164N, red), with prominent sources indicated. Most bright stars are cluster members, except for CK 2, which is a well-known background red supergiant behind 46 magnitudes of visible extinction (Casali & Eiroa 1996). Also clearly visible is the outflow from the class 0 protostar SMM 3 (the source itself is not visible in the NIR). Dominating the reflection nebosity is the matter surrounding the class I binary EC 90 to the south and the Serpens Reflection Nebula to the north, which is transversed by the EC 82 disk shadow. The blue color of the EC 82 reflection nebula indicates that there is relatively little foreground extinction compared to the redder nebosity around EC 90. It is curious that another likely disk shadow is visible to the southeast of CK 2. This shadow surrounds the low-luminosity young star EC 123, coincidentally with almost the same position angle as the EC 82 shadow.

## 3. Analysis

The EC 82 disk shadow consists of two opposite lobes, one extending toward the northeast, and one extending to the southwest (henceforth referred to as the “eastern” and “western” lobes, respectively). Together, the shadow lobes have a position angle of  $\sim 50^\circ$  east of north. The shadow can be traced to a distance of more than 17,000 au ( $40''$ ) from the central source along each lobe, corresponding to a light-travel time of 0.27 yr, or almost 100 days.

Thus, a change in the geometry of the inner disk, or its central light source, on timescales longer than 100 days can lead to changes in the shadow across its full extent when comparing the two epochs. Conversely, changes in the disk taking place on timescales less than 100 days will manifest as changes over a smaller range of radii in the shadow, as the perturbation travels outwards at the speed of light. However, the shadow is best-defined within  $\sim 45$  days and  $\sim 75$  days in the western and eastern lobes, respectively, and we therefore restrict our quantitative analysis to 45 days. Given the angular resolution of HST at  $1.6 \mu\text{m}$  of  $0''.151$  (FWHM), the data in principle allow for the measurement of disk perturbations on timescales as short as 10 hr.

For the purpose of searching for variability, we compare the F160W (epoch 1) and F164N (epoch 2) filters, as these have overlapping band passes. While the F164N filter includes coverage of the [Fe II] line at  $1.64 \mu\text{m}$ , it is unlikely that any large-scale difference in the shadow morphology is due to line emission, and we interpret the observed differences as being due to a change in broad wavelength illumination.

Because the reflecting cloud contains significant substructure, changes in the shadow morphology are most apparent in differential or relative measurements between the two epochs. This is illustrated in Figure 2, which shows the  $1.6 \mu\text{m}$  ratio image between the two epochs (2017 July/2018 August). The ratio image highlights the shadow as the dominant source of variability in the region. The most apparent change is that each lobe has changed its position angle across the full extent of the shadow by several degrees, and that the position angle change has occurred in opposite angular directions for the two lobes. That is, the western lobe moved in a clockwise direction, whereas the eastern lobe moved in a counter-clockwise direction between 2017 and 2018. The two shadow lobes are therefore not co-planar, with the 2017 epoch being more out-of-plane than the 2018 epoch. This is unequivocal evidence for non-axisymmetry of the system, although we cannot immediately distinguish between a non-axisymmetry of the disk itself, or of the illuminating source (see Section 4).

### 3.1. Retrieval of Time-dependent Disk Parameters

In this analysis, we quantify the time-dependence of disk structure by retrieving basic structural parameters as a function of time, based on equidistant cross sections of the shadow. We model the shadow using a simple pressure-supported and viscous disk model of the form (Hartmann et al. 1998):

$$\rho_d(R, \theta) = \frac{\Sigma_d(R)}{\sqrt{2\pi} h_R R} \times \exp\left[-\frac{1}{2}((\pi/2 - \theta)/h_R)^2\right], \quad (1)$$

where  $h_R = H/R$  is the disk scale height  $H$  at radius  $R$ , in units of  $R$ , and  $\theta$  is the polar angle measured from the axis of rotation. The scale height is parameterized as  $h_R(R) = h_R(R_{\text{outer}}) \times (R/R_{\text{outer}})^\psi$ . The dust surface density profile is

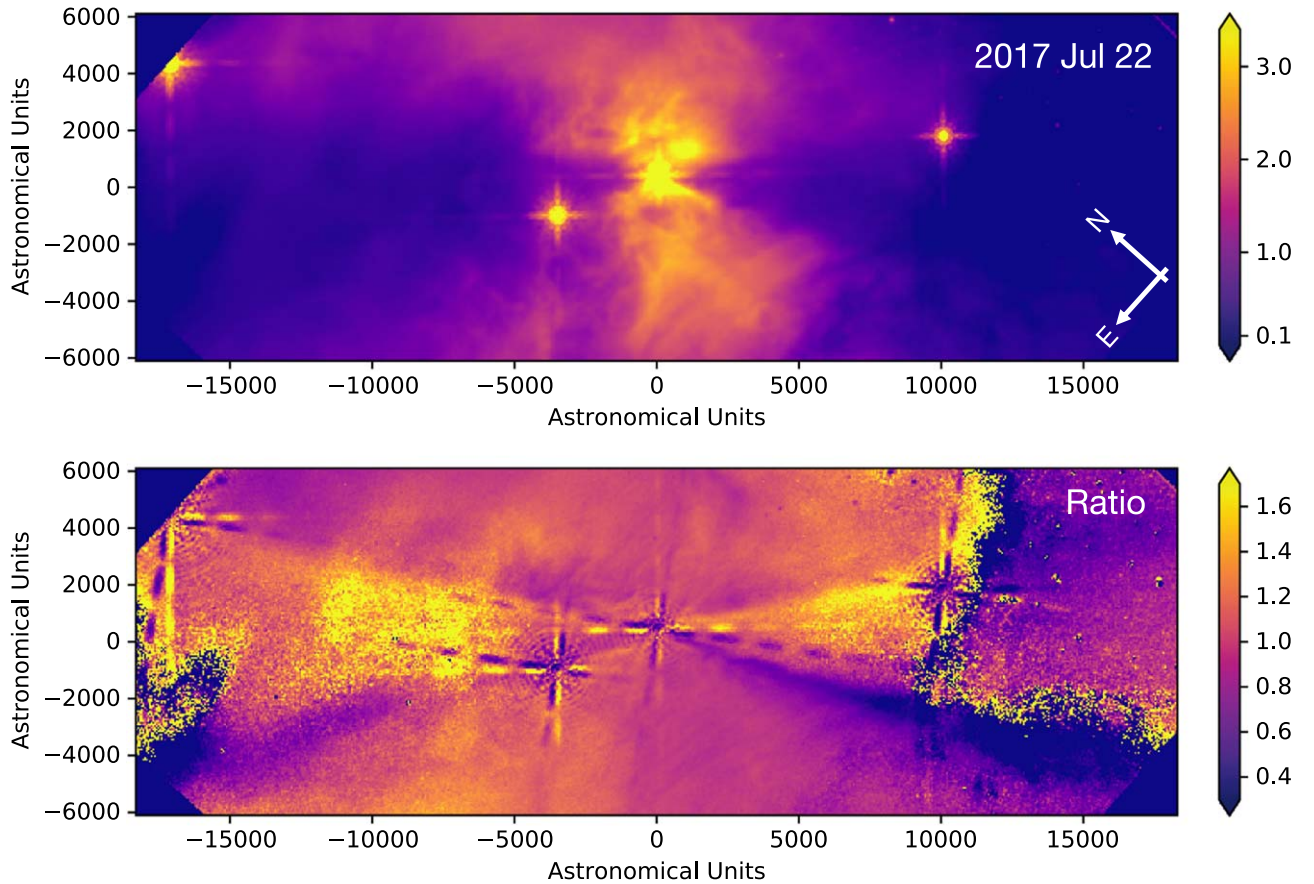


**Figure 2.** Top panel: rotated and scaled  $1.6 \mu\text{m}$  images of EC 82 for the two observing epochs, presented as an animation. The animation flips between the two epochs (2017 July/2018 August) five times in its 10 s run time. The color scale is logarithmic and scaled to the same arbitrary unit to emphasize the shadow morphology. Bottom panel: the  $1.6 \mu\text{m}$  ratio image of the two epochs, with lighter colors indicating higher ratio. The resulting ratio image highlights the change in angle of the two shadow lobes. It also demonstrates that the change in angle happens in opposite directions for the two lobes.

(An animation of this figure is available.)

also a power law,  $\Sigma_d(R) \propto R^\gamma$ . This formulation uses the approximation that the vertical coordinate  $z = R \sin(\pi/2 - \theta) \simeq R(\pi/2 - \theta)$ , appropriate for  $\theta \simeq \pi/2$ . The optical depth profile,  $\tau$ , is then a one-dimensional function of  $\theta$ :

$$\tau(\theta) = \int_{R_{\text{inner}}}^{R_{\text{outer}}} \rho(R, \theta) C_{\text{ext}} dR. \quad (2)$$

$C_{\text{ext}}$  is the extinction coefficient at the observing wavelength,  $\lambda$ . This model assumes single scattering, but in practice the shadow is probably partly filled in either by multiple scattering, or by scattering of photons from other sources. Further, the distribution of scattering dust is not uniform. We therefore model the intensity profile of the shadow by adding a linear continuum, as well as a linear background component:

$$I(\theta) = (I_C(\theta) - I_{\text{BG}}) \times \exp(-\tau) + I_{\text{BG}}, \quad (3)$$

where  $I_{\text{BG}} = A_{\text{BG}} + B_{\text{BG}} \times \theta$ . Finally, the intensity profile is convolved by a one-dimensional Gaussian kernel with a FWHM of  $0''.151$  to simulate the WFC3 point-spread function at  $1.6 \mu\text{m}$ . We generally assume uninformative, or flat, priors for all parameters. The single exception is that we let the linear continuum be fixed, defined by the surface brightness on each side of the shadow, corresponding to a highly constrained prior.

However, we do assume a flat prior for the background component.

We use `emcee` (Foreman-Mackey et al. 2013) to sample the posterior probability distribution of the model parameters. Because we wish to search for temporal variations in the shadow geometry within a single epoch, as well as between epochs, we retrieve independent probability distributions of slices of constant distance of the shadow from the source. To minimize the effect of any artifacts, we average each slice over 10 pixels in the radial direction. This translates into a time-resolution of  $10 \times 0''.08 = 0''.8 = 2.0$  days.

For each slice, we use the following standard likelihood function:

$$\ln(L) = -\frac{1}{2}(R^T C^{-1} R + \ln(\det(C)) + N_{\text{pix}} \ln(2\pi)), \quad (4)$$

where  $R = \text{Data} - \text{Model}$  is the residual and  $C$  is the covariance matrix for the pixel errors.

A representative corner plot for one of the slices is shown in Figure 3 and an example fit is shown in Figure 4. The probability distributions demonstrate that many parameters are degenerate, including the flaring index, as well as the inner and outer radii, but also that the disk scale height and position angle are well-determined. These are the two parameters that can be monitored over time. Finally, the background intensity is

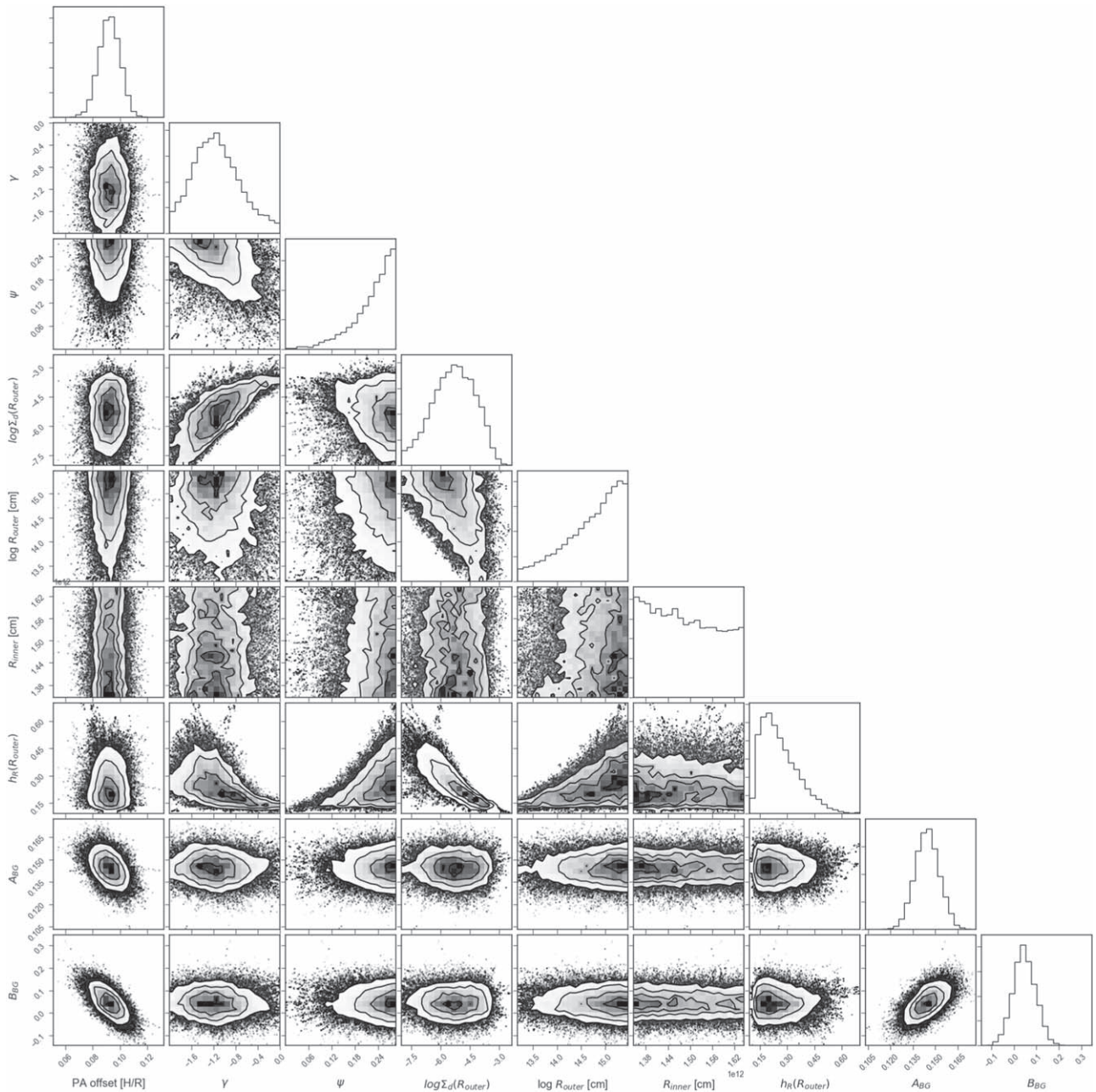


**Figure 3.** Representative corner plot for the western lobe, epoch 2 at a distance of  $7''2$  from EC 82, corresponding to 18.1 days. The corner plot demonstrates that the position angle offset (in units of  $H/R$ ) is well-constrained, as is the background level, and the disk scale height,  $(H/R)_0$ . The radial surface density power law is consistent with an  $R^{-1}$  dependence. Conversely, the inner and outer radii of the disk are not well-constrained. This plot made use of `corner.py` (Foreman-Mackey 2016).

well-determined, although its slope correlates somewhat with the shadow position angle.

### 3.2. Quantified Shadow Variability

The subset of constrained parameters are summarized in Figure 5. They include the position angle, the disk scale height, and the background intensity. The data for the two epochs are overlaid as a function of light-travel time relative to the time of observation. It is seen that there are features present in all parameters, and that these features reappear at the same relative light-travel time in both epochs. Because of this invariance, we interpret these features as being due to intrinsic physical structure in the scattering cloud, rather than properties of the

shadow. For instance, there is a prominent offset in the position angle around 11–17 days in the western lobe, which is directly visible in the image as well. Because these physical structures have size scales of  $\gtrsim 1000$  au, it is not expected that they will vary significantly over a 1 yr timescale, as is indeed supported by their recurrence in both epochs. However, any relative difference between the two epochs, at a given distance, may be interpreted as being due to variations in the shadow illumination, in turn implying a corresponding variation in the disk structure.

The strongest indicator of variability is the shadow position angle. In Figure 6, the relative difference between the retrieved position angles is shown for both the eastern and western lobes (epoch 2–epoch 1). Because we only have two epochs

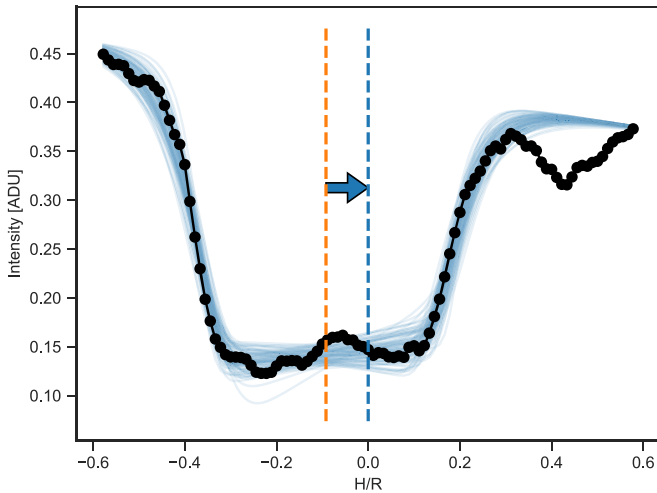


**Figure 4.** Samples of converged models (blue lines) overlaid on the data (black line and points) for the same slice used for the corner plot in Figure 3. The arrow indicates the direction and magnitude of the retrieved angular offset of the shadow model, equivalent to a relative position angle.

available, and the cloud features tend to be as strong as any shadow variability, we are not able to assign any relative difference to one epoch over the other.

While the eastern lobe position angle is less certain due to the presence of a bright stellar source in the shadow, this metric recovers the trend seen in the ratio map in Figure 2 in which a clockwise shift in the western lobe (negative change in position angle) is matched by a counter-clockwise shift in the eastern lobe (positive change in position angle). Further, the western lobe displays a clear trend toward increasing negative angles as a function of time, moving the shadow from  $\sim -1$ deg to  $\sim -5$ deg. Colloquially, one may think of the observed shadow variability as being reminiscent of the flapping of a bird’s wings. We rule out that proper motion of the entire system leads to the shadow variability, as this would imply unphysically high velocities. Indeed, toward the outer edge of the shadow, the observed change is in excess of 1000 au. Over the epoch separation of 404 days, this would correspond to a velocity of more than  $4000 \text{ km s}^{-1}$ .

There is not sufficient temporal coverage to detect any periodicity in the variation of the position angle. During the  $\sim 45$  days of detectable change available within a single image, the western lobe position angle changes in a manner consistent with a linear trend with time. That is, if there is periodicity in the variation, the period is at least  $\sim 4 \times 45 = 180$  days. Using Kepler’s law, and assuming a stellar mass of  $2.5 M_{\odot}$ , this corresponds to a semimajor axis of  $\gtrsim 0.85$  au. At the same time, a period is unlikely to be much greater than this, as an extrapolation of a sinusoidal signature would lead to position angle changes much larger than a few degrees, which is not seen in previous images of the Serpens shadow (e.g., Gorlova et al. 2010; Sugitani et al. 2010). Consequently, we find that the variability is consistent with orbital motion at  $\gtrsim 1$  au and up to a few au, subject to confirmation by more extensive monitoring.

Apart from the position angle, we can also look for changes in disk scale height. However, while Figure 5 shows variation in the retrieved scale height, the repeated pattern in the two epochs suggest that this variation is also dominated by the underlying cloud structure, rather than in shadow variability. Indeed, there is no significant indication of a systematic, relative difference in scale height between the two epochs, also

not where the position angle difference is the greatest. The retrieved disk scale heights vary between  $H/R = 0.15$ – $0.5$ . The extreme ends of this range are probably dominated by cloud structure, but the preferred median of  $H/R = 0.25 \pm 0.05$  can be interpreted as representative for the disk. While this disk scale height is much larger than that expected for a continuous flaring disk at 1 au (Dullemond & Dominik 2004), it is roughly consistent with the height of a directly irradiated puffed-up inner rim at the same radius (Dullemond et al. 2001). Conversely, the shadow from a flared disk will be dominated by the outer disk scale height at large radii ( $\sim 20$ – $100$  au for a typical disk; Hendlar et al. 2020), but this is inconsistent with the short timescale of the variation. We therefore suggest that the shadowing material is dominated by a puffed-up inner disk, implying that the outer disk is self-shadowed, and that the short-term variability of the large shadow is evidence of self-shadowing within the disk itself.

### 3.3. Evolutionary Stage of EC 82

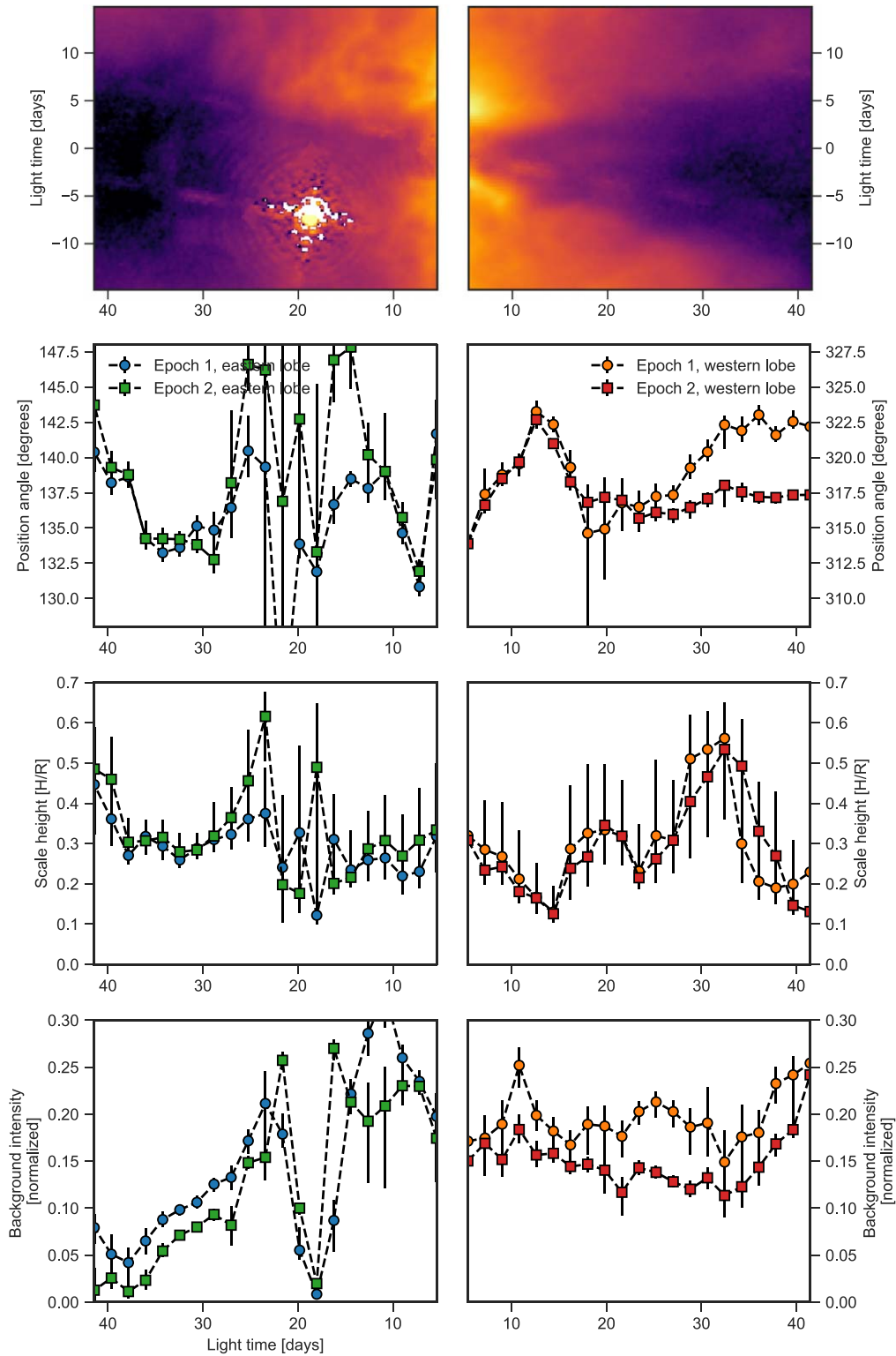
The properties and evolutionary stage of EC 82 are uncertain, in part due to the fact that its edge-on disk obscures the central star, decreases its apparent luminosity, and changes the shape of the SED of the star-disk system. While it has long been thought that the central star is a solar-mass object, the recently revised distance to Serpens of  $\sim 436$  pc (Ortiz-León et al. 2017) increases the luminosity of EC 82 to  $30 L_{\odot}$ , making it likely that EC 82 is actually an intermediate-mass star.

Figure 7 shows the SED of EC 82, including the Herschel PACS spectra obtained from the COPS-DIGIT-FOOSH archive (Green et al. 2016), and superimposed on the best-fitting model from Pontoppidan & Dullemond (2005). The 2–24  $\mu\text{m}$  logarithmic spectral index defined as:

$$\alpha = \frac{d \log \lambda F_{\lambda}}{d \log \lambda} = 0.3 \quad (5)$$

formally identifies the source as a class I object (Dunham et al. 2015). However, this identification is confounded by the edge-on geometry, which suppresses the short-wavelength range of the SED. The presence of strong 10 and 20  $\mu\text{m}$  silicate emission features are difficult to reconcile with the presence of any substantial protostellar envelope, which would invariably create deep silicate and ice absorption features due to the presence of significant column densities of cold dust toward the central infrared source (Robitaille et al. 2007). Consequently, if EC 82 were viewed at a more face-on angle, it is likely to display an SED typical for a protoplanetary disk. In the context of the Herbig stars, it is difficult to predict if the face-on SED would be typical of Group I (flared) or II (self-shadowed) disks (Meeus et al. 2001; Acke et al. 2009). Since the shadow is likely to be formed at small radii, based on the short timescale for the shadow variability, EC 82 disk is likely self-shadowed at large radii.

Is EC 82 a classical, full disk, or a more evolved, transitional disk? The system appears to have significant amounts of hot material (up to 1500 K) near the central star, as evidenced by strong veiling at 1–2  $\mu\text{m}$  (Doppmann et al. 2005; Gorlova et al. 2010), strong mid-infrared silicate emission, and strong rovibrational CO emission lines (Banzatti & Pontoppidan 2015). The mid-infrared slope of the SED is flat (see Figure 5 and Dunham et al. 2015), indicative of a full disk. Pontoppidan



**Figure 5.** Summary of constrained parameters as a function of light-travel time. The top panels show the epoch 2 image (F164N), while the lower three rows show the retrieved position angles, disk scale heights, and background intensities, respectively. Each epoch is indicated by a different color and symbol. The western lobe is much better defined, as the eastern lobe is strongly affected by the presence of a bright source (EC 86).

& Dullemond (2005) found that it was difficult to model the strong silicate emission features while considering the edge-on orientation and the presence of a large surrounding reflection nebula. Their solution was to model the system using a very low-mass disk ( $M_{\text{disk}} \sim 10^{-5} M_{\odot}$ ), indicative of a highly evolved system similar to a debris disk, and a flat density

distribution of the surrounding cloud. Finally, this model found that the reflection nebula corresponds to a NIR extinction of  $A_J = 1.4$  mag along the line of sight, estimated both by the SED fit, as well as the observed depth of the  $3.08 \mu\text{m}$  water ice absorption band. In this work, we do not attempt to re-fit the radiative transfer model, but note that the new PACS spectra

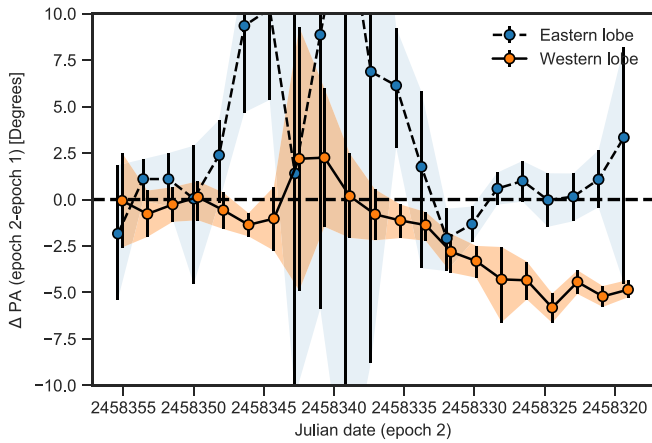


**Figure 6.** Relative change in position angle between the two epochs as a function of Epoch 2 date. The values for each lobes are offset relative to each other by one day, for clarity.

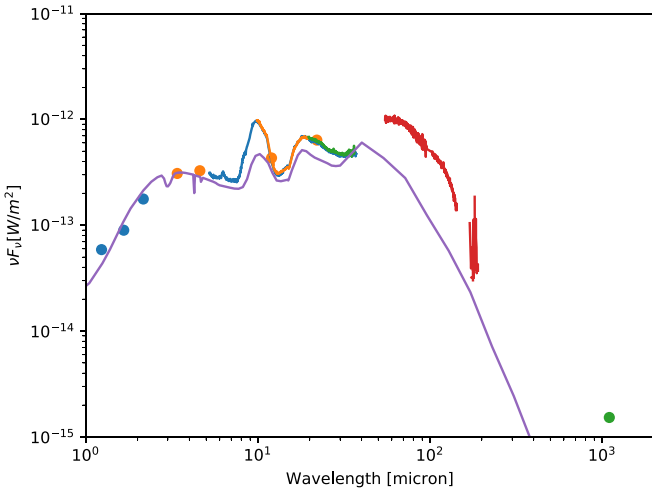


**Figure 7.** Observed spectral energy distribution of EC 82. The data include photometry from 2MASS, WISE (Dunham et al. 2015), and spectroscopy from Spitzer (Pontoppidan et al. 2010; Lebouteiller et al. 2011) and Herschel (Green et al. 2016). The solid curve shows the model from Pontoppidan & Dullemond (2005), derived before the PACS spectroscopy was available.

and millimeter photometry point to a more massive outer disk than that proposed in Pontoppidan & Dullemond (2005), making it more likely that EC 82 is a classical protoplanetary disk. However, adding a more massive outer disk while still fitting the strong emission features from the inner disk may require the use of a flat, self-shadowed outer disk component.

## 4. Discussion

### 4.1. Shadow Variability Due to an Inner Disk Warp

The hydrodynamics of protoplanetary disks govern both star- and planet-formation, but are difficult to constrain by direct observation. Even with high-resolution imaging, typically only a snapshot in time is available. Traditional tracers of disk dynamics include instantaneous velocity structure using high-resolution line spectroscopy (Hughes et al. 2011; Teague et al. 2019), or indirect accretion diagnostics, such as hydrogen recombination lines (Muzerolle et al. 1998; Salyk et al. 2013). In this paper, we have shown that giant disk shadows may be used to provide a continuous measure of disk motions with <1 day resolution using a combination of relatively infrequent

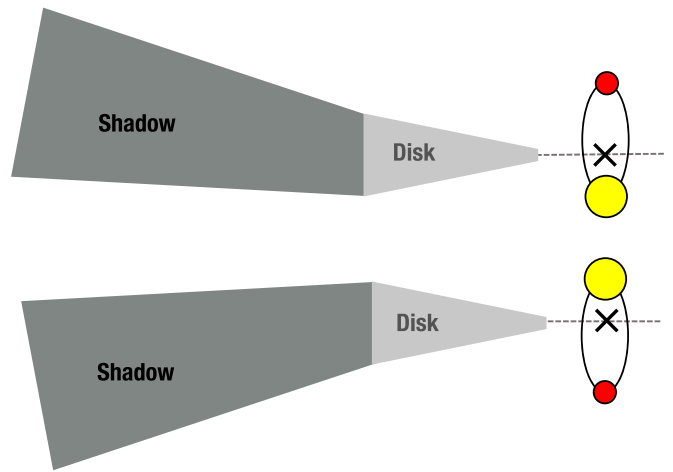


**Figure 8.** Sketch showing an alternative explanation for the shadow variability, in which an unequal-mass binary orbiting out of the disk plane shifts the photocenter of the illumination. This predicts that the inner disk is cleared-out of material and that the position angle variation is strongly periodic. The sketch is not to scale.

(every 40–50 days) imaging and the finite light-travel time across the shadow. A drawback is that giant disk shadows, such as that in Serpens, are rare, and are thus only available for a very small number of disks.

Of particular interest is the potential for strong periodicity in the shadow position angle, as this may indicate an origin in interactions with a low-mass companion, including planetary-mass objects. If the variability is due to a forced perturbation, e.g., from a low-mass companion or planet, strong periodicity is likely. However, the anti-symmetry of the position angle change (the “flapping”) in the two lobes suggests a quadrupolar disk warp rather than the bipolar warp that is typically seen in misaligned inner disks (Juhász & Facchini 2017; Facchini et al. 2018); a change in a bipolar warp would produce a symmetric “wobble.” It is not presently clear if there is a theoretical basis for such a quadrupolar warp, and further modeling is required to test this idea.

### 4.2. Shadow Variability Due to a Low-mass Companion

We have discussed a model in which the variability is caused by an orbiting, or precessing, quadrupolar disk warp. Since this is a phenomenological explanation in need of theoretical confirmation, it is not entirely satisfactory. However, there is an alternative explanation: a low-mass companion to EC 82, orbiting out of the plane of the disk, may move the photocenter of the source relative to the disk plane. This would also lead to non-planar (flapping) change in observed shadow position angle. This scenario is illustrated in Figure 8. It requires an unequal-mass (or unequal-luminosity) binary, as an equal-mass binary would not move the photocenter at any point in its orbit.

The main argument against a stellar binary is that this scenario could be at odds with the presence of an optically thick inner disk, as evidenced by the SED of the system (see Section 3.3). That is, a low-mass stellar companion on a  $\gtrsim 160$  day orbit may clear the inner several au of any material, leaving a deficit in the mid-infrared parts of the SED (Cieza et al. 2010). However, there are examples of circumbinary disks where each component is associated with significant amounts of hot dust; examples include binaries such as HD 142527 (Lacour et al. 2016) and GG Tau (Beust & Dutrey 2005), with relatively large

semimajor axes ( $\gtrsim 15$  au) and correspondingly decades-long periods. Binaries with smaller separations tend to have less hot material, but there are notable exceptions such as the triple system GW Ori, which includes an inner binary with a semimajor axis of 1.25 au and a period of 241 days (Czekala et al. 2017), coupled with an SED showing strong silicate emission, similar to that of EC 82 (Fang et al. 2014). Further, the dynamic action of such a close binary on the disk itself is likely significant, so this does not exclude that part of the variability is still due to a disk warp, in this case induced by a stellar binary.

There is, to our knowledge, no current evidence for a spectroscopic binary in EC 82, but the available stellar spectroscopy is not constraining due to the presence of strong veiling (Doppmann et al. 2005). Consequently, we cannot rule out, based on current knowledge, that the variability is due to the out-of-plane binary orbit of an unequal-mass binary. However, this scenario predicts consistent and strong periodicity of the shadow position angle, and can therefore be excluded if future monitoring fails to detect such a periodic signature.

## 5. Conclusion

We have found that the giant disk shadow projected by the young star EC 82 in the Serpens core is variable. In particular, the position angle of the shadowing material relative to the stellar photocenter changes by several degrees over timescales of a year. The large angular size of the shadow corresponds to a light-travel time of more than 45 days, allowing for detailed constraints on the dynamics of the EC 82 disk using the magnification effect of the long shadow. Because the variability timescale is relatively short, we conclude that the occulting material is located within a few au of the central star, and that any disk component at larger radii is likely self-shadowed. We suggest that further monitoring of the disk shadow from a stable platform such as Hubble, or the upcoming James Webb Space Telescope, offers a unique opportunity to constrain, in real time, the hydrodynamics of terrestrial planet-forming regions. Based on just two epochs of imaging, we cannot determine if the variability is periodic, and further imaging on a months to years cadence is required to establish, or reject, periodicity and a potential connection to a low-mass perturber.

This work is based on observations made with the NASA/ESA Hubble Space Telescope, obtained from the Mikulski Archive for Space Telescopes (MAST) at the Space Telescope Science Institute. The specific observations analyzed can be accessed via doi:10.17909/t9-ws22-gb68. STScI is operated by the Association of Universities for Research in Astronomy, Inc. under NASA contract NAS 5-26555. This work is based in part on observations made with the Spitzer Space Telescope, which was operated by the Jet Propulsion Laboratory, California Institute of Technology under a contract with NASA. Herschel is an ESA space observatory with science instruments provided by European-led Principal Investigator consortia and with important participation from NASA. K.M.P. and T.P. are supported by a NASA ROSES XRP grant NNX17AB60G S005.

*Facilities:* HST(WFC3), WISE, 2MASS, Herschel(PACS), Spitzer(IRS).

*Software:* This paper made use of the *astropy* package (Astropy Collaboration et al. 2013), *matplotlib* (Hunter 2007), the *emcee* package by Foreman-Mackey et al. (2013), and *DrizzlePac* (STSCI Development Team 2012).

## ORCID iDs

Klaus M. Pontoppidan  <https://orcid.org/0000-0001-7552-1562>

Joel D. Green  <https://orcid.org/0000-0003-1665-5709>

Tyler A. Pauly  <https://orcid.org/0000-0001-9500-9267>

Colette Salyk  <https://orcid.org/0000-0003-3682-6632>

## References

- Acke, B., Min, M., van den Ancker, M. E., et al. 2009, *A&A*, 502, L17  
 Astropy Collaboration, Robitaille, T. P., Tollerud, E. J., et al. 2013, *A&A*, 558, A33  
 Banzatti, A., & Pontoppidan, K. M. 2015, *ApJ*, 809, 167  
 Benisty, M., Juhász, A., Facchini, S., et al. 2018, *A&A*, 619, A171  
 Beust, H., & Dutrey, A. 2005, *A&A*, 439, 585  
 Britt, C. T., Maccarone, T. J., Green, J. D., et al. 2016, *MNRAS*, 460, 2822  
 Burrows, C. J., Stapelfeldt, K. R., Watson, A. M., et al. 1996, *ApJ*, 473, 437  
 Casali, M. M., & Eiroa, C. 1996, *A&A*, 306, 427  
 Casassus, S., Avenhaus, H., Pérez, S., et al. 2018, *MNRAS*, 477, 5104  
 Cieza, L. A., Schreiber, M. R., Romero, G. A., et al. 2010, *ApJ*, 712, 925  
 Czekala, I., Andrews, S. M., Torres, G., et al. 2017, *ApJ*, 851, 132  
 Debes, J. H., Poteet, C. A., Jang-Condell, H., et al. 2017, *ApJ*, 835, 205  
 Dong, R. 2015, *ApJ*, 810, 6  
 Doppmann, G. W., Greene, T. P., Covey, K. R., et al. 2005, *AJ*, 130, 1145  
 Duchêne, G., McCabe, C., Pinte, C., et al. 2010, *ApJ*, 712, 112  
 Dullemond, C. P., & Dominik, C. 2004, *A&A*, 417, 159  
 Dullemond, C. P., Dominik, C., & Natta, A. 2001, *ApJ*, 560, 957  
 Dunham, M. M., Allen, L. E., Evans, N. J., et al. 2015, *ApJS*, 220, 11  
 Facchini, S., Juhász, A., & Lodato, G. 2018, *MNRAS*, 473, 4459  
 Fang, M., Sicilia-Aguilar, A., Roccatagliata, V., et al. 2014, *A&A*, 570, A118  
 Foreman-Mackey, D. 2016, *JOSS*, 1, 24  
 Foreman-Mackey, D., Hogg, D. W., Lang, D., et al. 2013, *PASP*, 125, 306  
 Gorlova, N., Steinhauer, A., & Lada, E. 2010, *ApJ*, 716, 634  
 Green, J. D., Yang, Y.-L., Evans, N. J., et al. 2016, *AJ*, 151, 75  
 Hartmann, L., Calvet, N., Gullbring, E., et al. 1998, *ApJ*, 495, 385  
 Hendler, N., Pascucci, I., Pinilla, P., et al. 2020, *ApJ*, 895, 126  
 Hodapp, K. W., Walker, C. H., Reipurth, B., et al. 2004, *ApJL*, 601, L79  
 Hughes, A. M., Wilner, D. J., Andrews, S. M., et al. 2011, *ApJ*, 727, 85  
 Hunter, J. D. 2007, *CSE*, 9, 90  
 Juhász, A., & Facchini, S. 2017, *MNRAS*, 466, 4053  
 Kenyon, S. J., & Hartmann, L. 1995, *ApJS*, 101, 117  
 Kraus, A. L., & Hillenbrand, L. A. 2008, *ApJL*, 686, L111  
 Lacour, S., Biller, B., Cheetham, A., et al. 2016, *A&A*, 590, A90  
 Leboutteiller, V., Barry, D. J., Spoon, H. W. W., et al. 2011, *ApJS*, 196, 8  
 Marino, S., Perez, S., & Casassus, S. 2015, *ApJL*, 798, L44  
 Meeus, G., Waters, L. B. F. M., Bouwman, J., et al. 2001, *A&A*, 365, 476  
 Muzerolle, J., Hartmann, L., & Calvet, N. 1998, *AJ*, 116, 2965  
 O'dell, C. R. 1998, *AJ*, 115, 263  
 Ortiz-León, G. N., Dzib, S. A., Kounkel, M. A., et al. 2017, *ApJ*, 834, 143  
 Pinilla, P., Benisty, M., de Boer, J., et al. 2018, *ApJ*, 868, 85  
 Pontoppidan, K. M., & Dullemond, C. P. 2005, *A&A*, 435, 595  
 Pontoppidan, K. M., Salyk, C., Blake, G. A., et al. 2010, *ApJ*, 720, 887  
 Robitaille, T. P., Whitney, B. A., Indebetouw, R., et al. 2007, *ApJS*, 169, 328  
 Salyk, C., Herczeg, G. J., Brown, J. M., et al. 2013, *ApJ*, 769, 21  
 Siess, L., Dufour, E., & Forestini, M. 2000, *A&A*, 358, 593  
 Stapelfeldt, K. R., Krist, J. E., Ménard, F., et al. 1998, *ApJL*, 502, L65  
 STSCI Development Team 2012, *DrizzlePac*: HST Image Software, version 2.2.6, Astrophysics Source Code Library, ascl:1212.011  
 Sugitani, K., Nakamura, F., Tamura, M., et al. 2010, *ApJ*, 716, 299  
 Teague, R., Bae, J., & Bergin, E. A. 2019, *Natur*, 574, 378  
 Watson, A. M., & Stapelfeldt, K. R. 2007, *AJ*, 133, 845  
 Winston, E., Megeath, S. T., Wolk, S. J., et al. 2009, *AJ*, 137, 4777  
 Zari, E., Brown, A. G. A., & de Zeeuw, P. T. 2019, *A&A*, 628, A123